STRUCTURAL BIOLOGY

TRPV3 activation by different agonists accompanied by lipid dissociation from the vanilloid site

Kirill D. Nadezhdin, Arthur Neuberger, Lena S. Khosrof, Irina A. Talyzina, Jeffrey Khau, Maria V. Yelshanskaya, Alexander I. Sobolevsky*

TRPV3 represents both temperature- and ligand-activated transient receptor potential (TRP) channel. Physiologically relevant opening of TRPV3 channels by heat has been captured structurally, while opening by agonists has only been observed in structures of mutant channels. Here, we present cryo-EM structures that illuminate opening and inactivation of wild-type human TRPV3 in response to binding of two types of agonists: either the natural cannabinoid tetrahydrocannabivarin (THCV) or synthetic agonist 2-aminoethoxydiphenylborane (2-APB). We found that THCV binds to the vanilloid site, while 2-APB binds to the S1-S4 base and ARD-TMD linker sites. Despite binding to distally located sites, both agonists induce similar pore opening and cause dissociation of a lipid that occupies the vanilloid site in their absence. Our results uncover different but converging allosteric pathways through which small-molecule agonists activate TRPV3 and provide a framework for drug design and understanding the role of lipids in ion channel function.

INTRODUCTION

Transient receptor potential (TRP) channels are cellular detectors of physical and chemical stimuli in the environment, including temperature, pressure, pH, and lipid composition of the cellular membrane. There are 28 members of the TRP channel superfamily, divided into seven subfamilies based on similarity in their amino acid sequences and conserved structural architecture and features (*1*–*4*). The cation-selective channel TRPV3 is a member of the vanilloid subfamily (TRPV1 to TRPV6) of TRP channels, which is mainly expressed in skin cells called keratinocytes (*5*). TRPV3 regulates skin homeostasis (*6*), hair development (*7*, *8*), and formation of the epidermal barrier (*9*), and is associated with various skin conditions, such as itch (*10*), atopic dermatitis (*11*), and rosacea (*12*), as well as rare genetic disorders like Olmsted syndrome (*13*–*15*).

TRP channels are mostly known for their ability to detect changes in temperature. Eleven of the 28 TRP channels, including TRPV3, are temperature sensitive and referred to as thermo-TRPs (*16*–*18*). In contrast to other thermo-TRPs, activation of TRPV3 can be enhanced by repetitive stimulation by either heat or exposure to agonists in a process called sensitization (*5*, *19*, *20*). Like many other TRP channels or ion channels in general, TRPV3 function is modulated by specific lipids such as arachidonic acid (*21*), cholesterol (*22*), and phosphatidylinositol 4,5-bisphosphate (PIP_2) (*23*). However, unlike other representatives of the vanilloid-subfamily TRP channels (TRPVs) TRPV1, TRPV5, and TRPV6 (*24*), which are regulated by phosphatidylinositol (PI), PIP_2, and cholesterol, respectively, no specific type of lipid has been found essential for TRPV3 function.

The mechanisms of TRPV3 gating, including channel opening, have been addressed by previous structural studies (*25*–*30*). While temperature activation was successfully monitored by opening the mouse TRPV3 channel in response to heat exposure (*26*, *29*), application of small-molecule agonists has yet to open wild-type TRPV3 channels. The Y564A mutation was necessary to open mouse TRPV3 by agonist 2-APB (*25*), while the K169A mutation caused opening of human TRPV3, either in the presence of 2-APB (*31*) or in the absence of any agonists (*28*). Because these so-called sensitizing mutations introduce substantial changes in the energetics of TRPV3 gating, uncovering the physiologically relevant mechanism of ligand-induced activation requires solving open-state structures of wild-type TRPV3. Wild-type channel structures can also serve as more reliable templates for the design of drugs targeting TRPV3 in pathological conditions.

To investigate the molecular mechanism of TRPV3 activation by small molecules, we solved cryo–electron microscopy (cryo-EM) structures of human TRPV3 in complex with agonists tetrahydrocannabivarin (THCV) and 2-aminoethoxydiphenylborane (2-APB). We found that THCV binds to the vanilloid site where it outcompetes an endogenous lipid. While 2-APB binds to two different sites, distal from the THCV binding site, it also causes dissociation of lipid from the vanilloid site, in this case allosterically. Both THCV and 2-APB not only induce similar pore opening but also cause TRPV3 inactivation. We employed mutagenesis and calcium uptake measurements to confirm the binding sites of THCV and 2-APB and proposed two different but converging molecular mechanisms of agonist-induced TRPV3 activation and inactivation.

RESULTS

Structural characterization and activation of TRPV3 by small-molecule agonists

We purified wild-type human TRPV3 protein, incorporated into cNW30 circularized lipid nanodiscs, and subjected it to cryo-EM. In the absence of ligands, the sample revealed a single population of TRPV3 particles that yielded a 2.46-Å resolution three-dimensional (3D) reconstruction (Fig. 1A, figs. S1 and S2, and table S1). We built the corresponding structural model of the apo-state (APO), which has a similar fold to other TRPVs and includes a transmembrane domain (TMD) with the central ion channel pore and an intracellular skirt that is mostly built of ankyrin repeat domains (ARDs) connected by three-stranded β sheets (Fig. 1B). We also modeled several nonprotein densities per subunit around the TMD (Fig. 1A) as annular lipids.

Department of Biochemistry and Molecular Biophysics, Columbia University, New York, NY, USA.
*Corresponding author. Email: as4005@cumc.columbia.edu

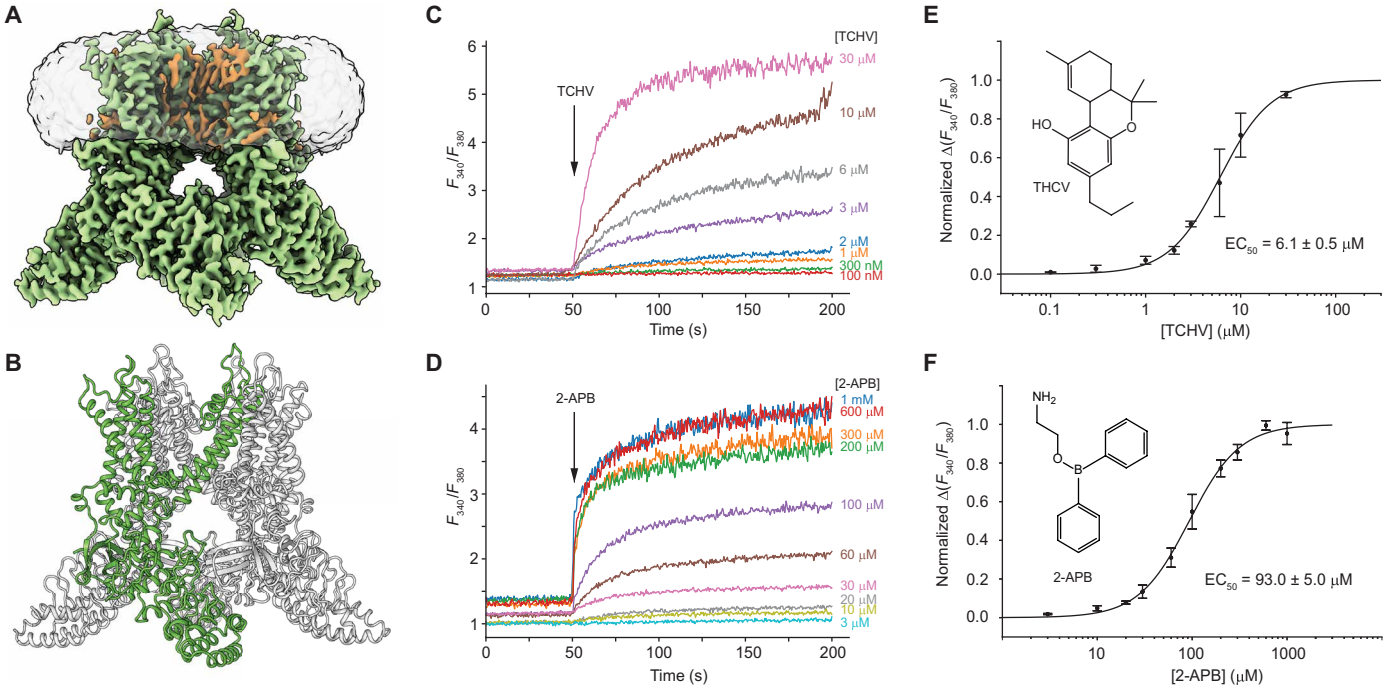

Fig. 1. Apo-state structure in cNW30 nanodisc and TRPV3 activation by agonists. (**A**) Cryo-EM density map of human TRPV3 in the closed, apo state at 2.46-Å resolution, viewed parallel to the membrane. Lipid densities are colored brown. The semitransparent surface represents the lipid nanodisc density. (**B**) Structural model of $TRPV3_{apo}$ viewed parallel to the membrane. One of the four subunits is colored green, while the others are colored gray. (**C** and **D**) Representative ratiometric Fura-2AM–based fluorescence measurements of changes in intracellular Ca^{2+} for human embryonic kidney (HEK) 293S GnTI$^-$ cells expressing wild-type human TRPV3. Changes in the fluorescence intensity ratio at 340 and 380 nm (F_{340}/F_{380}) were monitored in response to application of agonists THCV (C) or 2-APB (D) at different concentrations. (**E** and **F**) Concentration dependencies of TRPV3 activation by THCV (E) and 2-APB (F). Changes in the F_{340}/F_{380} ratio were normalized to its maximal value at saturating agonist concentrations and fitted with the logistic equation (black lines), with half-maximal effective concentration (EC_{50}) = 6.1 ± 0.5 μM and n_{Hill} = 1.63 ± 0.13 for THCV (E; n = 3 independent experiments) and EC_{50} = 93.0 ± 5.0 μM and n_{Hill} = 1.63 ± 0.11 for 2-APB (F; n = 6 independent experiments). Data are means ± SEM. The insets show chemical structures of THCV (E) and 2-APB (F). Source data are provided.

We tested activation of TRPV3 functionally by expressing these channels in human embryonic kidney (HEK) 293S cells and evaluating TRPV3-mediated Ca^{2+} uptake using ratiometric measurements of changes in Fura-2AM fluorescence in response to application of THCV (Fig. 1C) or 2-APB (Fig. 1D). THCV induced concentration-dependent activation of TRPV3 with the half-maximal effective concentration (EC_{50}) = 6.1 ± 0.5 μM (n = 3; Fig. 1E and table S2). Likewise, 2-APB activated TRPV3 with EC_{50} = 93 ± 5 μM (n = 6; Fig. 1F and table S2). Therefore, our experiments confirmed the ability of both THCV and 2-APB agonists to effectively activate wild-type human TRPV3, in full agreement with previous observations (*32*, *33*).

TRPV3 structures in complex with the cannabinoid THCV

We determined structures of wild-type human TRPV3 in complex with THCV by subjecting the purified protein reconstituted in cNW30 circularized lipid nanodiscs to cryo-EM in the presence of 100 μM THCV. Data analysis revealed two distinct classes of particles that yielded 3.68- and 3.63-Å resolution reconstructions of the channel in the open, $OPEN_{THCV}$, and inactivated or desensitized, $INACT_{THCV}$, states (figs. S2 and S3 and table S1). Between "inactivated" and "desensitized," we chose to use the term inactivated to be consistent with the nomenclature introduced in the previous cryo-EM studies of TRPV2 (*34*) and TRPV3 (*28*). Thus, in whole-cell patch-clamp recordings, the existence of this inactivated state for wild-type and mutant human TRPV3 was demonstrated by a current decline in the continuous presence of agonist (*28*).

The corresponding structures had similar overall architectures to the apo-state structure but revealed four nonprotein densities (one per TRPV3 protomer) with the distinct shape of THCV (Fig. 2, A to E) located in the vanilloid binding pocket (*24*, *35*, *36*) formed by the S3, S4, and S4-S5 linkers of one subunit (residues W521, F522, L557, A560, N561, and L563) and the S5-S6 region of the neighboring subunit (residues F601, T660, and L664) (Fig. 2B). These densities appeared nearly identical between $OPEN_{THCV}$ and $INACT_{THCV}$ and were modeled by THCV molecules (Fig. 2, C to E). Although no ligands were previously reported to bind to the vanilloid site in wild-type TRPV3 (only lipids), amino acid substitutions in this site yielded a mutant channel sensitive to resiniferatoxin (*37*).

To verify the identified THCV site (site 1) functionally, we mutated residues contributing to THCV binding and compared THCV-induced activation of wild-type and mutant TRPV3 channels using Ca^{2+} uptake measurements (Fig. 2F and table S2). While these measurements do not discriminate between the effects of mutations on gating and agonist binding, they provide a gross assessment of changes in the agonist activating potency. Compared to wild-type TRPV3 (EC_{50} = 6.1 ± 0.5 μM, n = 3), the activating potency of THCV, estimated from normalized changes in the fluorescence intensity ratio

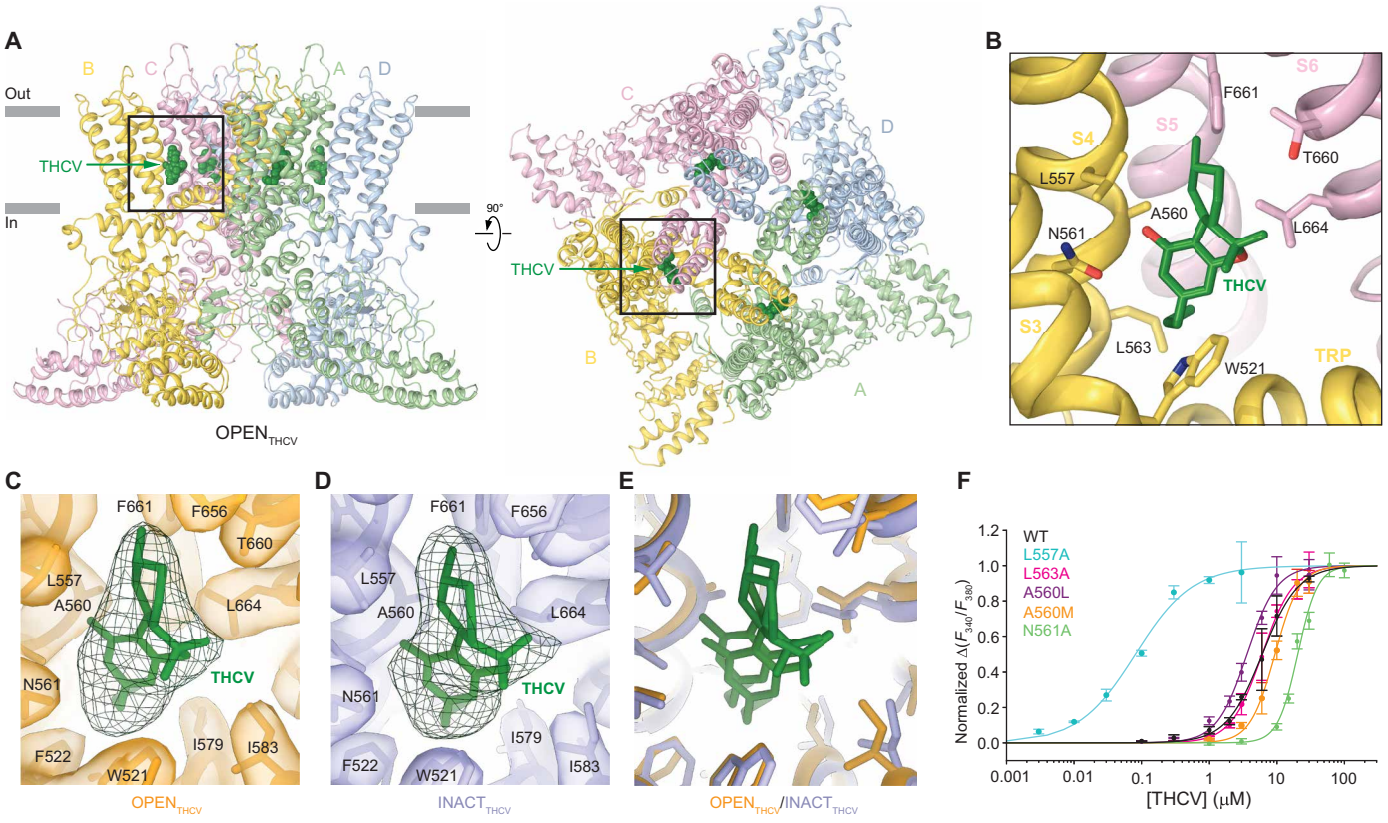

Fig. 2. Binding of THCV to the vanilloid site. (**A**) Structure of OPEN$_{THCV}$ viewed parallel to the membrane (left) and extracellularly (right), with subunits colored light green, yellow, pink, and blue. The molecules of THCV are shown as space-filling models (dark green). Boxed is the region expanded in (**B**). (B) Close-up view of the vanilloid site in OPEN$_{THCV}$ structure, with the molecule of THCV (dark green) and side chains contributing to THCV binding shown in sticks. (**C** to **E**) Close-up views of the vanilloid site in OPEN$_{THCV}$ (C), INACT$_{THCV}$ (D), and their superposition (E), with cryo-EM densities for the protein (semitransparent surface) and THCV (green mesh) shown in (C) and (D). (**F**) Concentration-response curves for THCV activation of wild-type (WT) TRPV3 (black, $n = 3$) as well as L557A (cyan, $n = 3$), L563A (pink, $n = 3$), A560L (purple, $n = 3$), A560M (orange, $n = 3$), and N561A (green, $n = 3$) mutant channels. Curves through the data points are the fits with the logistic equation. The EC_{50} values are provided in table S2. *n*, the number of independent measurements. Data are means ± SEM.

at 340 and 380 nm (F_{340}/F_{380}), was markedly increased for the L557A mutant ($EC_{50} = 0.081 \pm 0.001$ μM, $n = 3$), while substantially weakened for N561A ($EC_{50} = 24.4 \pm 1.7$ μM, $n = 3$). The marked reduction in the value of EC_{50} for L557A was not accompanied by changes in the maximum absolute value of the fluorescence intensity ratio (5.29 ± 0.04, $n = 3$ for wild type, and 5.58 ± 0.47, $n = 3$ for L557A, $P = 0.61$ in the two-sample *t* test), suggesting that this mutation altered the agonist affinity but not efficacy. Therefore, the results of mutagenesis combined with functional recordings support the prediction that THCV-induced activation and inactivation of TRPV3 is mediated by binding of THCV to the vanilloid site.

Protein conformations in THCV-induced open and inactivated states

Compared to APO, OPEN$_{THCV}$ and INACT$_{THCV}$ exhibited several structural differences. Globally, the intracellular skirt of OPEN$_{THCV}$ moved ~5 Å toward the membrane compared to APO and INACT$_{THCV}$ and rotated by ~8° clockwise around the central symmetry axis when viewed intracellularly (Fig. 3, A to C). Similar overall changes were previously observed during opening of mutant mouse or human TRPV3 activated by 2-APB (*25*, *28*, *31*) or mouse TRPV3 activated by heat (*26*, *29*). As a signature of ion channel activation, the pore in OPEN$_{THCV}$ (Fig. 3, E and H) became much wider than in APO (Fig. 3, D and G) or INACT$_{THCV}$ (Fig. 3, F and I). Measurements of the pore radius demonstrated that the gate region in OPEN$_{THCV}$ is expanded compared to the apo state and has a similar size to the gate region in the most open mutant mouse or human TRPV3 channels (*25*, *28*, *31*) or wild-type mouse TRPV3 channel activated by heat (fig. S4), which was shown to readily permeate water and cations during molecular dynamics simulations (*29*).

The pore's narrowest constriction at the gate region of APO and OPEN$_{THCV}$ is formed by side chains of four (one per subunit) isoleucines I674. In APO, these isoleucines create a hydrophobic seal within the pore, effectively blocking the permeation of ions and water. However, in OPEN$_{THCV}$, the isoleucines are spaced apart, allowing the passage of ions and water (Fig. 3, D, E, G, and H). The I674-containing S6 segments in APO and OPEN$_{THCV}$ have π-bulges in the middle. In contrast, the S6 segments in INACT$_{THCV}$ undergo a local π-to-α transition, making S6 entirely α-helical (Fig. 3, F and I). To accommodate this transition, the C-terminal portion of S6 rotates by ~100° and exposes leucines L673 and methionines M677 instead of I674 to the ion channel pore (Fig. 3, F and I), similar to the previously published structures of TRPV3 in the nonconducting inactivated state (*25*, *27*, *28*, *31*, *38*).

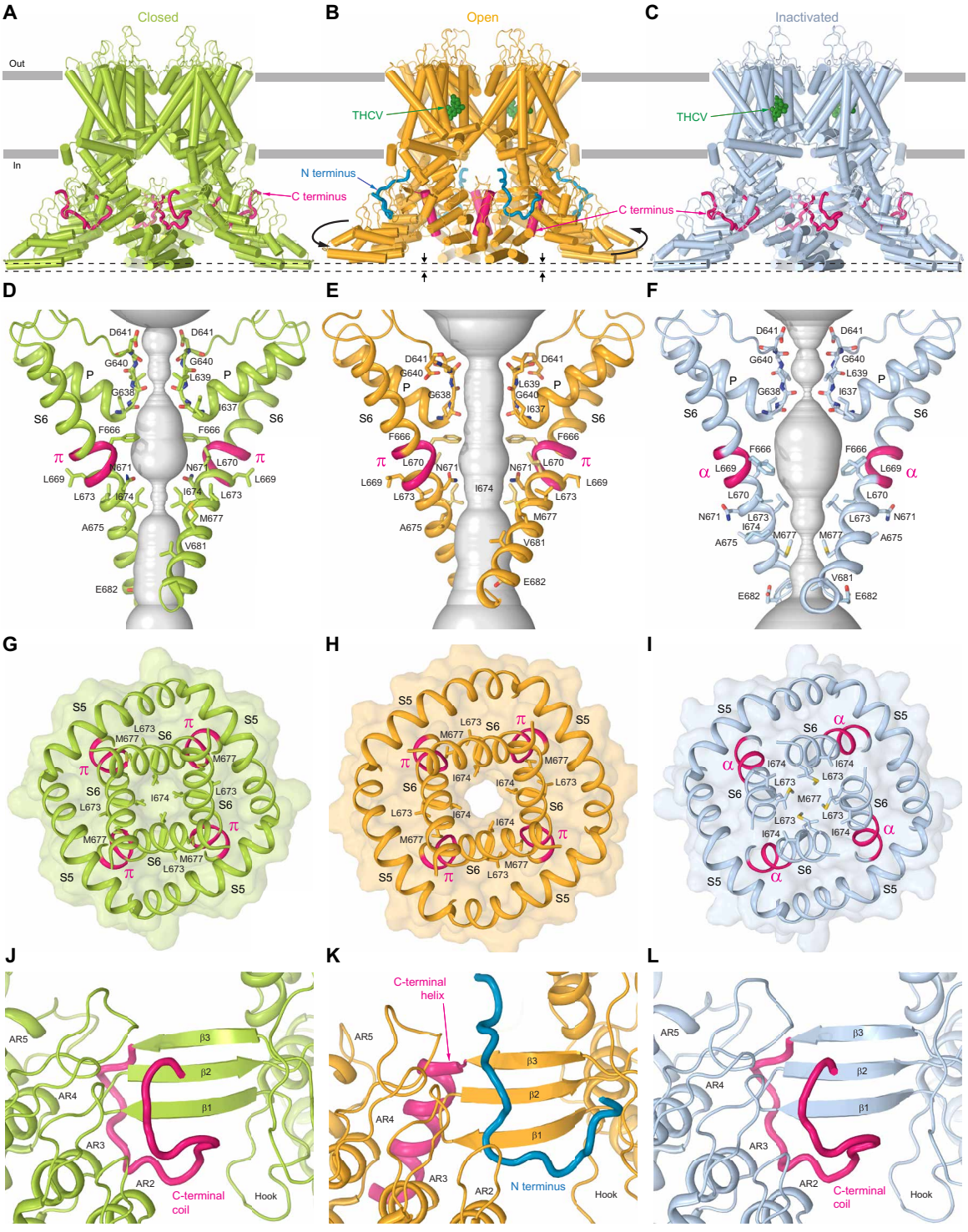

Fig. 3. Closed apo and THCV-bound open and inactivated states. (**A** to **C**) Structures of APO (A), $OPEN_{THCV}$ (B), and $INACT_{THCV}$ (C), viewed parallel to the membrane, with the N and C termini colored blue and pink, respectively, and the molecules of THCV (dark green) shown as space-filling models. (**D** to **F**) Pore-forming domains in APO (D), $OPEN_{THCV}$ (E), and $INACT_{THCV}$ (F), with residues contributing to pore lining shown as sticks. Only two of the four subunits are shown, with the front and back subunits omitted for clarity. The pore profile is shown as a space-filling model (gray). The region that undergoes the α-to-π transition in S6 is highlighted in pink. (**G** to **I**) Intracellular view of the S6 bundle crossing in APO (G), $OPEN_{THCV}$ (H), and $INACT_{THCV}$ (I), with the surface shown in the corresponding color. (**J** to **L**) Interface between the neighboring subunits in APO (A), $OPEN_{THCV}$ (B), and $INACT_{THCV}$ (C), with the C terminus (pink) adapting coiled [(J) and (L)] or helical (K) conformations and N terminus (blue) appearing in the open state (K).

The pore opening in $OPEN_{THCV}$ is also accompanied by changes in the conformations of the N and C termini. These conformational changes have been previously observed during opening of mutant mouse or human TRPV3 induced by 2-APB (*25*, *28*, *31*) or heat-induced activation of mouse TRPV3 (*26*, *29*). Thus, in the nonconducting APO or $INACT_{THCV}$, the C terminus forms a coil that wraps around the three-stranded β sheet and "glues" together the neighboring-subunit elements of the intracellular skirt (Fig. 3, J and L). In contrast, upon THCV-induced opening of wild-type human TRPV3, the C terminus unwraps and forms an α helix (Fig. 3K). The vacated cleft between the elements of the skirt becomes filled with the N terminus of the neighboring subunit, which is disordered in the nonconducting APO and $INACT_{THCV}$ (Fig. 3, J to L). The more pronounced intersubunit interfaces in $OPEN_{THCV}$ enforced by both N terminus– and C terminus–mediated interactions likely facilitate movements of the intracellular ARDs toward the membrane and their rotation around the axis of the fourfold symmetry (Fig. 3, A to C).

TRPV3 structures in complex with 2-APB

To study the structural mechanism of TRPV3 activation by 2-APB, we used the same protein sample preparation as described above but subjected TRPV3 to cryo-EM in the presence of 1 mM 2-APB. Similar to THCV, the cryo-EM data analysis identified two populations of particles in the presence of 2-APB representing distinct conformations of TRPV3. The corresponding 3D reconstructions yielded 2.59- and 2.83-Å resolution structures of the channel in the open, $OPEN_{2\text{-}APB}$, and inactivated, $INACT_{2\text{-}APB}$, states (figs. S2, S5, and S6 and table S1).

In contrast to wild-type human TRPV3 structures in complex with THCV, where one molecule of THCV binds to one TRPV3 subunit (four THCV molecules per TRPV3 tetramer), two molecules of 2-APB appear to bind to one TRPV3 protomer (eight 2-APB molecules per TRPV3 tetramer) (Fig. 4, A and B). However, none of the 2-APB molecules bind to the vanilloid site, indicating that the binding site for THCV (site 1) is different from the binding sites (sites 2 and 3) for 2-APB. The first 2-APB binding site (site 2) is also referred to as the S1-S4 base site (*24*) and is located between the lower portion of the S1-S4 bundle and the TRP helix (Fig. 4C). In this site, 2-APB is coordinated by the side chains of S444, F526, E501, K500, C496, M706, and F703. Tyrosine Y564 substitution with alanine results in a 20-fold increase in 2-APB potency in mouse TRPV3 (*25*). However, in human TRPV3, Y564 is not directly involved in the binding of 2-APB, despite being in close proximity to the ligand (~3.8 Å).

While the S1-S4 base site of 2-APB binding has been previously identified in mouse TRPV3 channel (*25*), it has not been reported in structures of mutant human TRPV3 channels (*28*, *31*). In contrast, the second 2-APB binding site (site 3), also known as the ARD-TMD linker site (*24*), was earlier predicted in mouse TRPV3 based on high-throughput mutagenesis (*33*) and later confirmed structurally in both human (*28*, *31*) and mouse (*25*) TRPV3. This site is contributed by the LH2 and pre-S1 elements of the ARD-TMD linker domain and the TRP helix in each individual TRPV3 subunit and involves residues R693, R496, H426, H430, L420, and T421 (Fig. 4D). A third binding site for 2-APB, known as the S1-S4 top site, was previously identified in mouse TRPV3 (*25*). This site has not been reported in human TRPV3 (*28*, *31*), and we do not see a density for the agonist molecule at the location homologous to mouse TRPV3. We conclude that the S1-S4 top site of 2-APB binding is unique to mouse TRPV3.

To verify the identified 2-APB binding sites (sites 2 and 3) functionally, we mutated residues contributing to 2-APB binding and compared 2-APB–induced activation of wild-type and mutant TRPV3 channels using Ca^{2+} uptake measurements. Compared to wild-type TRPV3 ($EC_{50} = 93.0 \pm 5.0$, $n = 6$), the 2-APB activating potency was enhanced ~3-fold for the C496A mutant ($EC_{50} = 34.6 \pm 3.1$ μM, $n = 3$) and ~9-fold for S444L ($EC_{50} = 10.6 \pm 0.8$ μM, $n = 3$), substantially weakened for L420A ($EC_{50} = 245 \pm 29$ μM, $n = 3$) and R693F ($EC_{50} = 499 \pm 28$ μM, $n = 3$), and almost completely abolished for E501A ($EC_{50} > 1$ mM, $n = 3$) (Fig. 4, E and F, and table S2). The loss of mouse TRPV3 sensitivity to 2-APB has recently been demonstrated in response to a serine mutation of the highly conserved glycine G573 in the S4-S5 linker, at the distal from site 2 and 3 location (*39*). While it is possible that mouse TRPV3 has an additional 2-APB binding site in the vicinity of G573, the effect of G573S mutation is likely due to active involvement of the S4-S5 linker in channel gating (*25*, *29*). Notably, in our experiments, while mutations introduced at either 2-APB binding site caused changes in TRPV3 activation by 2-APB, they had little effect on activation by THCV (table S2). Vice versa, mutations introduced at the THCV binding site had minimal effect on TRPV3 activation by 2-APB (table S2). Therefore, the results of mutagenesis combined with functional recordings provide strong support to $OPEN_{2\text{-}APB}$ and $INACT_{2\text{-}APB}$ structures, which demonstrate 2-APB binding to sites 2 and 3 that are distinct from the THCV binding site 1.

Similar conformations of THCV and 2-APB bound TRPV3

Comparison of $OPEN_{2\text{-}APB}$ and $INACT_{2\text{-}APB}$ (fig. S7) revealed the same differences between these structures as were seen between $OPEN_{THCV}$ and $INACT_{THCV}$ (Fig. 3). Compared to $INACT_{2\text{-}APB}$, the intracellular skirt of $OPEN_{2\text{-}APB}$ moves ~5 Å toward the membrane and rotates by ~8° clockwise around the axis of fourfold rotational symmetry when viewed intracellularly (fig. S7, A and B). The pore in $OPEN_{2\text{-}APB}$ is much wider than in $INACT_{2\text{-}APB}$, and while the pore's narrowest constriction at the gate region of the open channel is formed by side chains of isoleucines I674, it is formed by side chains of leucines L673 and methionines M677 in the inactivated channel (fig. S7, C to F). Accordingly, S6 in $OPEN_{2\text{-}APB}$ has a π-bulge in the middle, while S6 in $INACT_{2\text{-}APB}$ is entirely α-helical. Last, the intersubunit interface that connects the elements of the intracellular skirt in the inactivated channel is contributed by the C terminus that forms a coil and wraps around the three-stranded β sheet (fig. S7H). In contrast, the C terminus in $OPEN_{2\text{-}APB}$ unwraps and forms an α helix that interacts with the neighboring subunit much less extensively (fig. S7G). Instead, the vacated intersubunit cleft becomes filled with the N terminus of the neighboring subunit, which is disordered in the APO and $INACT_{2\text{-}APB}$ structures (fig. S7G).

Given similar structural characteristics of 2-APB– and THCV-bound structures, it appears that $OPEN_{2\text{-}APB}$ and $OPEN_{THCV}$ represent very similar open states, while $INACT_{2\text{-}APB}$ and $INACT_{THCV}$ very similar inactivated states (Fig. 5). Pairwise alignment of $OPEN_{2\text{-}APB}$ and $OPEN_{THCV}$ as well as $INACT_{2\text{-}APB}$ and $INACT_{THCV}$ resulted in the root mean square deviation values of 0.70 and 0.89 Å, respectively. However, while the open-state structures appear essentially the same (Fig. 5, A, C, and E), the inactivated-state structures do show slight structural differences in the pore domain (Fig. 5, B, D, and F). Particularly, there are movements of S6 and the P-loop, which are obvious when the structures are superimposed (Fig. 5, B and D).

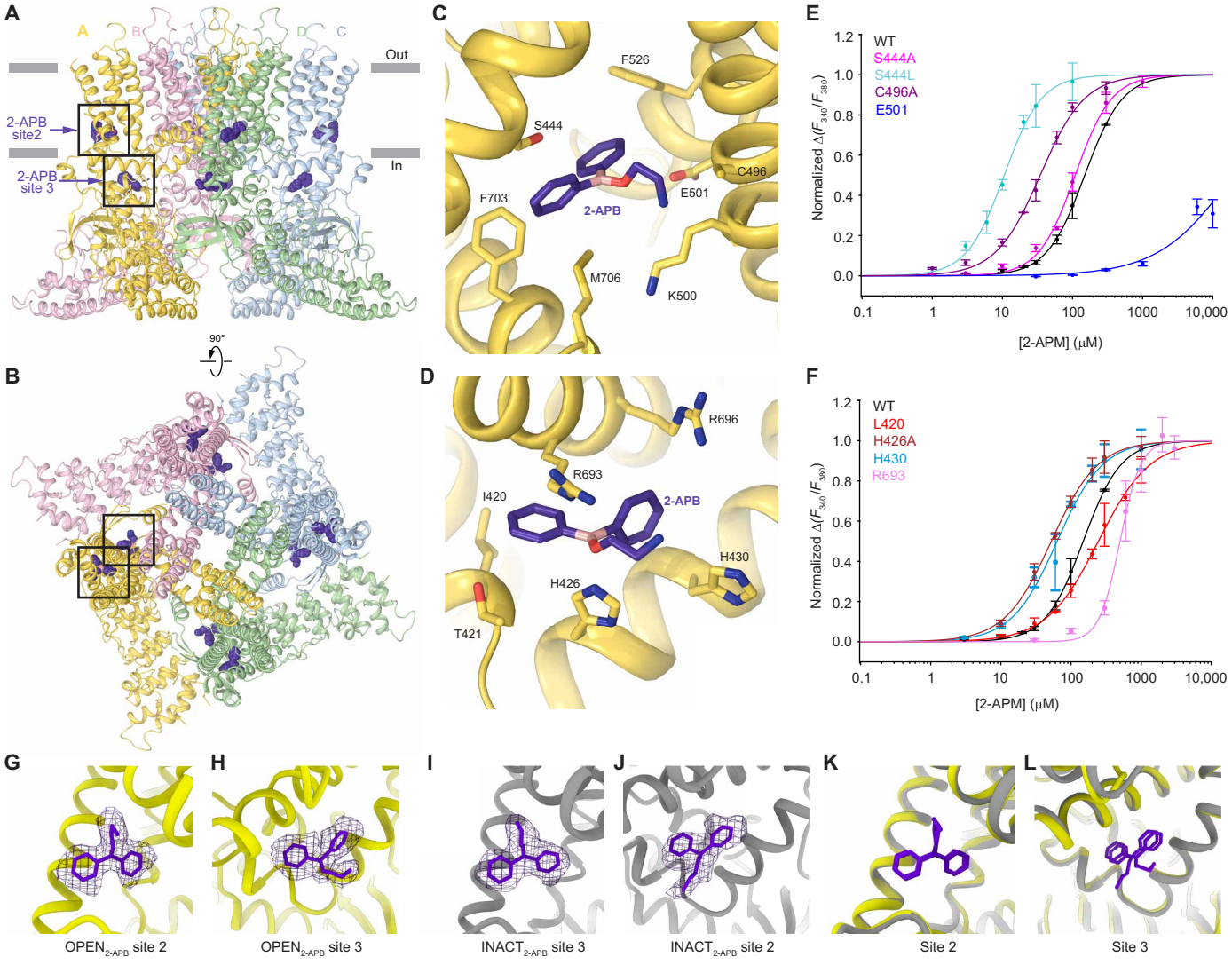

Fig. 4. Binding of 2-APB to the S1-S4 base and ARD-TMD linker sites. (**A** and **B**) Structure of $OPEN_{2\text{-APB}}$ viewed parallel to the membrane (A) and extracellularly (B), with subunits colored light green, yellow, pink, and blue. The molecules of 2-APB are shown as space-filling models (purple). Black rectangles indicate the regions expanded in (**C**) and (**D**). [(C) and (D)] Close-up views of the S1-S4 base (C) and ARD-TMD linker (D) sites in $OPEN_{2\text{-APB}}$ structure, with the molecule of 2-APB (purple) and side chains contributing to 2-APB binding shown in sticks. (**E** and **F**) Concentration-response curves for 2-APB activation of wild-type (black) and mutant (other colors) TRPV3 channels. Curves through the data points are the fits with the logistic equation. The EC_{50} values are provided in table S2. The number of independent measurements, *n*, equals to 6 for the wild-type channels and H426A mutant and equals to 3 for all other mutants. Data are means ± SEM. (**G** to **L**) Close-up views of the S1-S4 base [(G) and (I)] and ARD-TMD linker [(H) and (J)] sites in $OPEN_{2\text{-APB}}$ [(G) and (H)], $INACT_{2\text{-APB}}$ [(I) and (J)], and their superposition [(K) and (L)], with cryo-EM densities for 2-APB (purple mesh) shown in (G) to (J).

Nevertheless, these changes neither alter the overall structure (see Fig. 3 versus fig. S7) nor affect the critical signatures of the inactivated state, including the small size of the closed pore, the type of residues lining the gate region or the helical conformation of S6 (Fig. 5, B, D, and F). Our structural comparisons therefore suggest that the allosteric effects of THCV and 2-APB on TRPV3 appear to be the same despite these agonists acting through completely different binding sites (Fig. 5, A and B).

Dissociation of the vanilloid-site lipid upon agonist binding

Among annular lipids surrounding the TMD of human TRPV3 (Fig. 1A), there is a lipid that occupies the vanilloid site in the APO structure (Fig. 6, A and B). The vanilloid site was originally discovered in TRPV1, where it binds agonists, such as capsaicin or resiniferatoxin, competitive antagonists, like capsazepine and analgesic SB-366791, or PI lipid in the apo state (*35*, *36*, *40*–*43*). The active role of the vanilloid-site lipid was also proposed in temperature gating of TRPV1 (*36*, *41*) but was clearly demonstrated for the temperature gating of wild-type mouse TRPV3, where heat-induced channel opening was accompanied by the dissociation of this lipid (*29*). Similar to mouse TRPV3, the nature of the vanilloid-site lipid in our wild-type human TRPV3 structures remains ambiguous. Because we used 1-palmitoyl-2-oleoyl-glycero-3-phosphocholine (POPC) during TRPV3 reconstitution into nanodiscs (see Materials and Methods), we

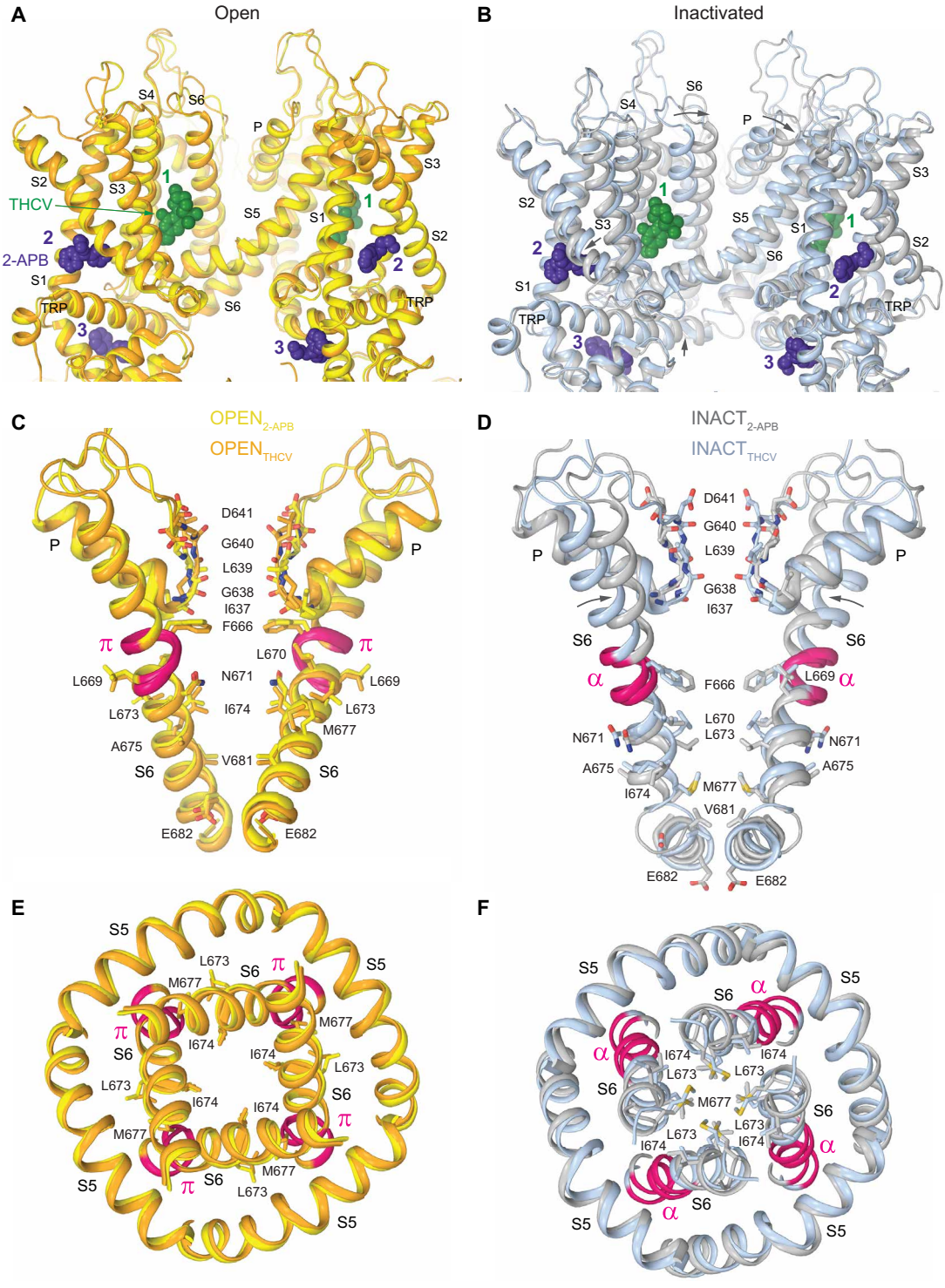

Fig. 5. THCV and 2-APB bind to different sites but induce similar pore conformations. (**A** and **B**) Superpositions of the TMDs in $OPEN_{2\text{-}APB}$ (yellow) and $OPEN_{THCV}$ (orange) (A) as well as $INACT_{2\text{-}APB}$ (gray) and $INACT_{THCV}$ (light blue) (B), viewed parallel to the membrane, with molecules of 2-APB (purple) and THCV (dark green) shown as space-filling models. Arrows show movement of domains in $INACT_{2\text{-}APB}$ relative to $INACT_{THCV}$. (**C** and **D**) Superpositions of the pore-forming domains in $OPEN_{2\text{-}APB}$ (yellow) and $OPEN_{THCV}$ (orange) (C) as well as $INACT_{2\text{-}APB}$ (gray) and $INACT_{THCV}$ (light blue) (D), with residues contributing to pore lining shown as sticks. Only two of the four subunits are shown, with the front and back subunits omitted for clarity. The region that undergoes the α-to-π transition in S6 is highlighted in pink. (**E** and **F**) Superpositions of the intracellular pore entry in $OPEN_{2\text{-}APB}$ (yellow) and $OPEN_{THCV}$ (orange) (E) as well as $INACT_{2\text{-}APB}$ (gray) and $INACT_{THCV}$ (light blue) (F), with residues contributing to the gate shown as sticks.

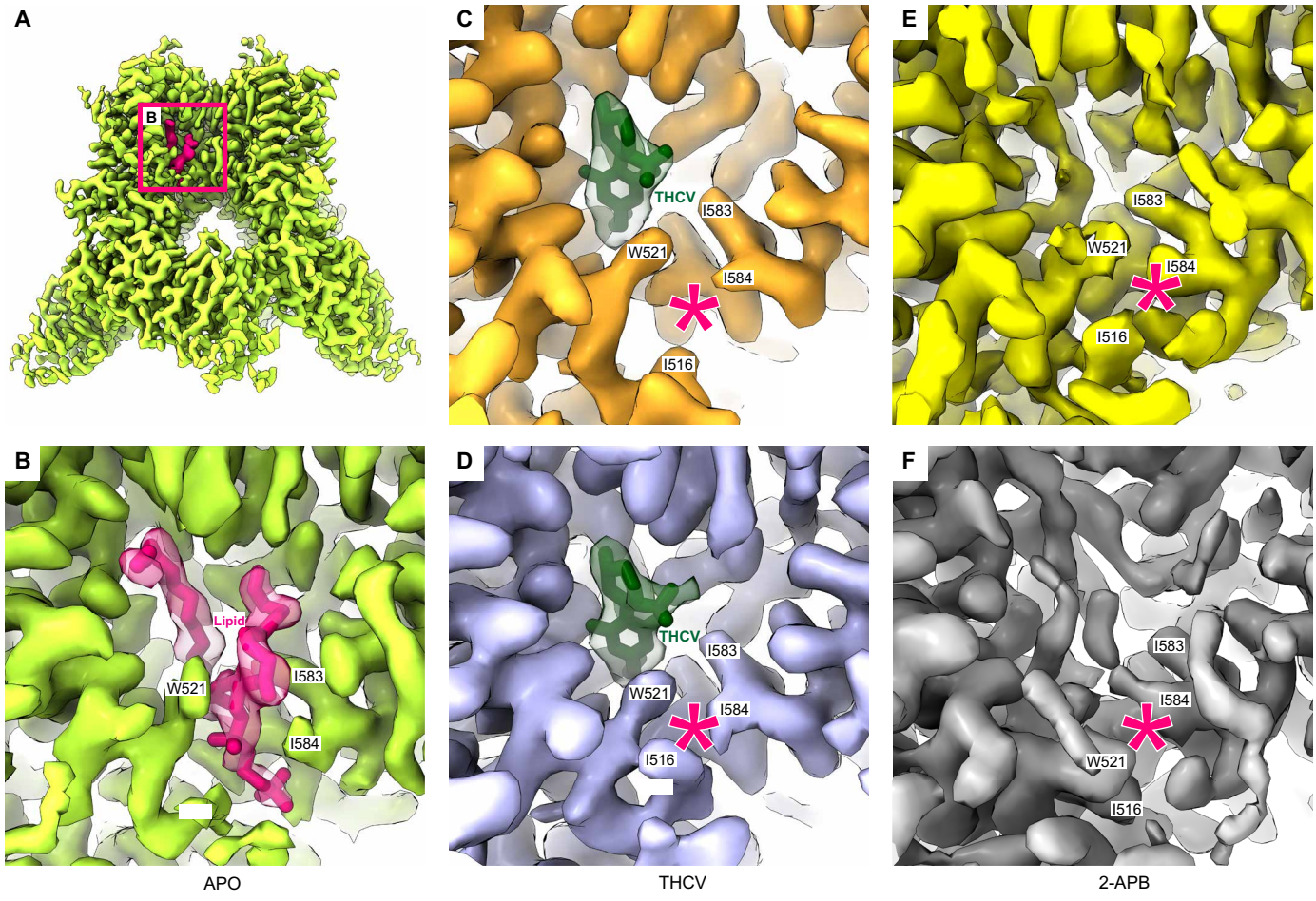

Fig. 6. Dissociation of the vanilloid-site lipid upon agonist binding. (**A**) Cryo-EM density for $TRPV3_{apo}$ (green), with the density for the vanilloid-site lipid colored in pink. Boxed is the region expanded in (**B**). (B) Close-up view of the vanilloid site in APO, with density for protein shown in green and resident lipid and its density in pink. (**C** and **D**) Close-up views of the vanilloid site in $OPEN_{THCV}$ (C) and $INACT_{THCV}$ (D), with density for protein shown in orange (C) and blue (D) and the molecule of THCV and its density in dark green. (**E** and **F**) Close-up views of the vanilloid site in $OPEN_{2\text{-}APB}$ (E) and $INACT_{2\text{-}APB}$ (F), with density for protein shown in yellow (E) and gray (F). The lack of the vanilloid-site lipid in (C) to (F) is indicated with asterisks.

modeled this lipid as phosphatidylcholine, but, as previously suggested by MD simulations of mouse TRPV3 (*29*), it can also represent other glycerophospholipids.

Because THCV binds to the vanilloid site (Fig. 2), this agonist appears to outcompete the lipid that resides in this site in the apo-state TRPV3 structure (Fig. 6, A and B). The vanilloid site in the $OPEN_{THCV}$ and $INACT_{THCV}$ structures only accommodates density for THCV, with no indications of lipid density (Fig. 6, C and D), and side chains of I516, W521, and I584 leave no room for extra density. The measured distance between Cε3 atom of W521 and Cδ1 atom of I584 is 4.4 Å in $OPEN_{THCV}$ and 8.8 Å in APO. While the agonist-induced dissociation of the vanilloid-site lipid is expected due to direct competition with THCV for the same site, it appears unexpected in the 2-APB–bound structures. Binding of 2-APB to the S1-S4 base and ARD-TMD linker sites (sites 2 and 3; Fig. 4), which are remote from the vanilloid site, also results in the vanilloid-site lipid dissociation in both $OPEN_{2\text{-}APB}$ and $INACT_{2\text{-}APB}$ structures (Fig. 6, E and F). This observation suggests that the vanilloid-site lipid plays an important role not only in temperature gating but also in ligand gating of the wild-type TRPV3 channels. Similarly, increased mobility of PI lipid in the vanilloid site was observed in the open-state structure of truncated TRPV1 bound to the toxin DkTx (*44*), suggesting that our conclusion might also be extended to other members of the TRP channel family.

DISCUSSION

We used cryo-EM to solve structures of full-length wild-type human TRPV3 in several states: closed (apo), THCV- or 2-APB–bound open, and agonist-bound inactivated states (Fig. 7). Despite THCV and 2-APB binding to different sites, our open-state structures, $OPEN_{THCV}$ and $OPEN_{2\text{-}APB}$, revealed the same conducting conformation of the ion channel. Likewise, our agonist-bound inactivated states, $INACT_{THCV}$ and $INACT_{2\text{-}APB}$, also exhibited a high degree of similarity. Collectively, our structures support the notion that allosteric TRPV3 agonists open and inactivate the channel in a similar manner, regardless of the binding site location.

We propose a three-state model of ligand-induced TRPV3 gating that includes closed, open, and inactivated states (Fig. 7). During the closed-to-open state transition in response to ligand binding, the

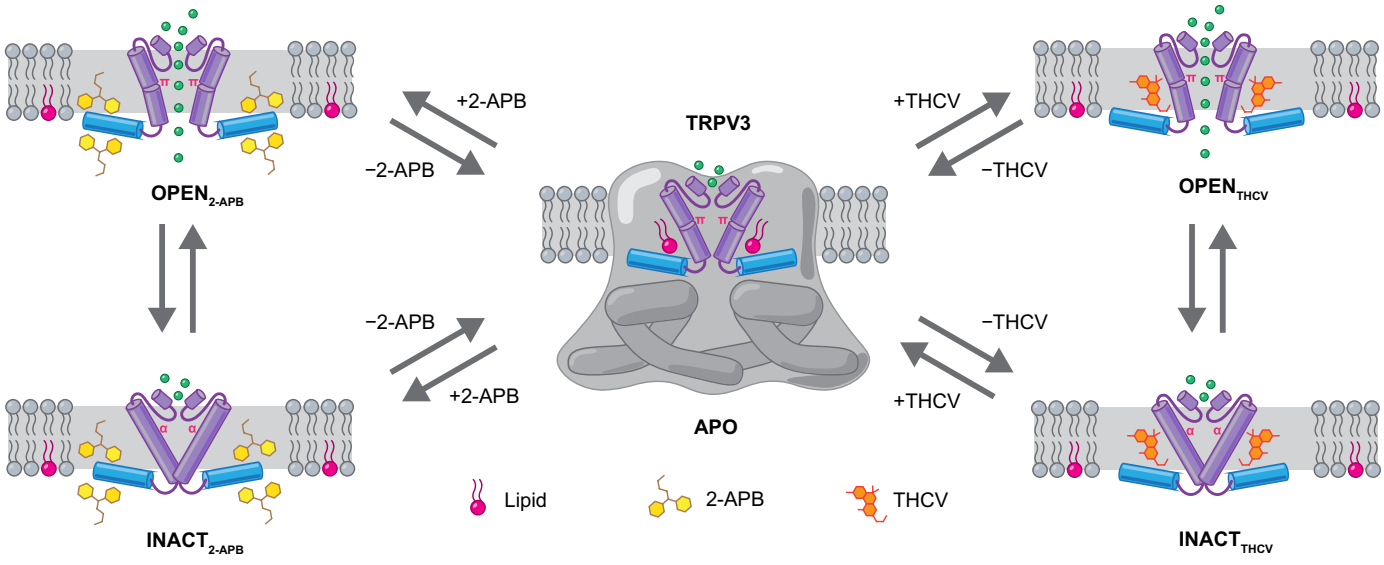

Fig. 7. Mechanism of agonist-induced TRPV3 activation. Schematic representation of TRPV3 in the closed, open, and inactivated states, with molecules of THCV and 2-APB agonists and vanilloid-site lipid shown in orange, yellow, and pink colors, respectively. Arrows indicate the putative interstate transitions. Green circles represent cations. The pore-forming regions (violet) and TRP helix (blue) are shown as cylinders. The final place of the dislocated vanilloid lipid is chosen arbitrary. Note that APO and OPEN conformations have a π-bulge in the middle of S6, while S6 in INACT is entirely α-helical.

channel experiences a set of conformational changes involving an ~8° rotation and ~5-Å movement of the intracellular skirt toward the membrane, expulsion of a lipid from the vanilloid pocket and dilation of the channel's pore for the passage of ions and water. During this transition, the C terminus unwraps the three-stranded β sheet connecting two adjacent TRPV3 subunits and forms an α helix (fig. S7G). In turn, the vacant intersubunit cleft becomes occupied with the N terminus of the neighboring subunit, which is disordered in the closed state. In contrast, by comparing the closed and inactivated states, all conformational changes are localized to the transmembrane region: the pore-forming S6 helices undergo a π-to-α transition, accommodated by a ~100° rotation of the C-terminal portion of S6 that exposes a completely different set of residues to the pore and seals it to ion and water permeation.

Previously, several TRPV3 structures reported ligand-bound open states, but all of them were determined for sensitized mutants, Y564A (*25*, *26*) or K169A (*28*), at moderate resolution. In addition, several available closed-state structures (*25*–*28*, *30*, *45*) can be classified into two groups based on the pore conformation. The first group includes structures with the π-bulge in the middle of S6 and the pore sealed by I674. The second group of structures has S6 being entirely α-helical and the pore sealed by M677. In the context of our three-state model, these first and second groups represent the APO and INACT states, respectively. It is clear, however, that our simplified model does not cover the full spectrum of TRPV3 conformations, including intermediate states. For example, in the presence of 2-APB, the K169A mutant was reported to adapt an unusual state with the π-bulge–containing S6 and α-helical C terminus (hallmarks of the open state) but with the channel pore sealed by M677 (signature of the inactivated state) (*28*, *31*). Additional studies are needed to decipher the full model of TRPV3 gating.

In conclusion, our high-resolution structures of wild-type human TRPV3 offer crucial insights into its gating mechanism. Furthermore, they serve as essential templates for structure-based drug design, enabling the modulation of TRPV3 activity in a state-dependent manner and facilitating the discovery of potential treatments for TRPV3-related channelopathies.

MATERIALS AND METHODS

Constructs

For structural experiments and Fura-2AM calcium imaging assay, cDNA for full-length wild-type human *TRPV3* (NM_001258205) (the corresponding protein residues 1 to 791) was introduced into *pEG-BacMam* vector for protein expression in mammalian cells (*46*), with an C-terminal region coding for the streptavidin affinity tag (residues WSHPQFEK), followed by the green fluorescent protein and the thrombin cleavage site (residues LVPRG), as described before (*47*, *48*). Point mutations in TRPV3 were introduced using standard molecular biology procedures.

Protein expression and purification

For cryo-EM studies, TRPV3 bacmids and baculoviruses were produced using the standard procedures (*46*). Briefly, baculovirus was made in Sf9 cells (Thermo Fisher Scientific, mycoplasma test negative; Gibco, no. 12659017) for ~96 hours and added to suspension-adapted HEK 293S cells lacking *N*-acetyl-glucosaminyltransferase I (GnTI$^-$, mycoplasma test negative; American Type Culture Collection, no. CRL-3022) that were maintained at 37°C and 6% CO_2 in FreeStyle 293 medium (Gibco–Life Technologies, no. 12338-018) supplemented with 2% fetal bovine serum. To enhance protein expression, sodium butyrate (10 mM) was added 24 hours after transduction, and the temperature was reduced to 30°C. The cells were harvested 48 hours after transduction by 15-min centrifugation at 5471*g* using a Sorvall Evolution RC centrifuge (Thermo Fisher Scientific). The cells were washed in the phosphate-buffered saline (pH 7.4) and pelleted by centrifugation at 3202*g* for 10 min using an Eppendorf 5810 centrifuge.

The cell pellet was resuspended in the ice-cold buffer containing 150 mM NaCl, 20 mM Tris-HCl (pH 8.0), 0.8 μM aprotinin, 4.3 μM leupeptin, 2 μM pepstatin A, 1 μM phenylmethylsulfonyl fluoride, and 1 mM β-mercaptoethanol (βME). The suspension was supplemented with 1% (w/v) glyco-diosgenin (GDN), and cells were lysed at constant stirring for 1.5 hours at 4°C. Unbroken cells and cell debris were pelleted in the Eppendorf 5810 centrifuge at 3202*g* and 4°C for 10 min. Insoluble material was removed by ultracentrifugation for 1 hour at 186,000*g* in a Beckman Coulter centrifuge using a 45 Ti rotor. The supernatant was added to the strep resin, which was then rotated for 20 min at 4°C. The resin was washed with 10 column volumes of wash buffer containing 150 mM NaCl, 20 mM Tris-HCl (pH 8.0), 1 mM βME, and 0.01% (w/v) GDN, and the protein was eluted with the same buffer supplemented with 2.5 mM D-desthiobiotin. The eluted protein was concentrated to 0.5 ml using a 100-kDa nominal molecular weight limit (NMWL) centrifugal filter (MilliporeSigma Amicon) and then centrifuged in a Sorvall MTX 150 Micro-Ultracentrifuge (Thermo Fisher Scientific) for 30 min at 66,000*g* and 4°C using a S100AT4 rotor before injecting it into a size exclusion chromatography (SEC) column. The protein was purified using a Superose 6 10/300 GL SEC column attached to an ÄKTA FPLC (GE Healthcare) and equilibrated with the buffer containing 150 mM NaCl, 20 mM Tris-HCl (pH 8.0), 1 mM βME, and 0.01% (w/v) GDN. The tetrameric peak fractions were pooled and concentrated to 2 to 3 mg/ml using a 100-kDa NMWL centrifugal filter (MilliporeSigma Amicon).

For TRPV3 reconstitution into cNW30 nanodiscs, the purified protein was mixed with circularized NW30 protein and lipids at a molar ratio of 1:3:166 (monomer:cNW30:lipid). POPC (Avanti Polar Lipids, USA) was used for the samples in apo conditions and in the presence of 2-APB, and soybean polar lipid extract (Avanti Polar Lipids, USA) was used for the samples in the presence of THCV. The cNW30 was stored in a buffer containing 150 mM NaCl, 20 mM Tris-HCl (pH 8.0), 1 mM *n*-dodecyl-β-maltoside at a concentration of 3.8 mg/ml. The lipids were resuspended to a concentration of 100 mg/ml in 150 mM NaCl and 20 mM Tris-HCl (pH 8.0) and subjected to 5 to 10 cycles of freezing in liquid nitrogen and thawing in a water bath sonicator. The nanodisc mixture (500 μl) was rocked at room temperature for 1 hour. Subsequently, the nanodisc mixture was supplemented with 40 mg of Bio-Beads SM2 (Bio-Rad) pre-wet in the buffer containing 150 mM NaCl and 20 mM Tris-HCl (pH 8.0) and subjected to rotation at 4°C. After 1 hour of rotation, 40 mg more of Bio-Beads SM2 was added, and the resulting mixture was rotated at 4°C for another ~14 to 20 hours. The Bio-Beads SM2 were then removed by pipetting, and TRPV3 reconstituted in nanodiscs was purified from empty nanodiscs by SEC using the Superose 6 10/300 GL column equilibrated in 150 mM NaCl, 20 mM Tris-HCl (pH 8.0), and 1 mM βME. The SEC fractions corresponding to TRPV3 reconstituted into nanodiscs were pooled and concentrated using 100-kDa NMWL centrifugal filter (MilliporeSigma Amicon) to 1.8 to 2.2 mg/ml.

Cryo-EM sample preparation and data collection

THCV was purchased from Cayman Chemical, and 2-APB was purchased from Thermo Scientific Chemicals. Both THCV and 2-APB were dissolved in dimethyl sulfoxide (DMSO) before their addition to the concentrated protein sample. To minimize the duration of TRPV3 incubation with THCV or 2-APB, we introduced the agonists into a sample containing TRPV3 reconstituted into cNW30 nanodiscs immediately before applying the sample to the grid. The total time of protein incubation with agonists before plunge-freezing was less than 1 min. Longer incubation times were not tested. The concentration of DMSO in samples after addition of agonists was in the range of 1 to 2% (v/v). Before sample application, CF 1.2/1.3, Au-50 (300-mesh) grids were plasma treated in a PELCO easiGlow glow discharge cleaning system (0.39 mBar, 15 mA, "glow" for 25 s, and "hold" for 10 s). A Mark IV Vitrobot (Thermo Fisher Scientific) set to 100% humidity at 22°C was used to plunge-freeze the grids in liquid ethane after applying 3 μl of protein sample to their gold-coated side using the blot time of 3 s, blot force of 3, and wait time of 15 s. The grids were stored in liquid nitrogen before imaging.

Images of frozen-hydrated particles of TRPV3 in apo conditions were collected at the Pacific Northwest Center for Cryo-EM (PNCC) on a Titan Krios transmission electron microscope (TEM) (Thermo Fisher Scientific) operating at 300 kV and equipped with a Gatan K3 direct electron detection (DED) camera (Gatan, Pleasanton, CA, USA). The total of 6621 micrographs were collected in the super-resolution mode with an image pixel size of 0.394 Å across the defocus range of −0.75 to −1.5 μm. The total dose of ~60 e^- Å^{-2} was attained by using the dose rate of ~18 e^- pixel^{-1} s^{-1} during the 2.064-s exposure time.

Images of frozen-hydrated particles of TRPV3 in the presence of 100 μM THCV were collected at the National Cryo-Electron Microscopy Facility (Frederick National Laboratory for Cancer Research) using the EPU software on a Titan Krios TEM operating at 300 kV and equipped with a post-column GIF Quantum energy filter and a Gatan K3 DED camera. The total of 9938 micrographs were collected in the counting mode with an image pixel size of 0.855 Å across the defocus range of −0.5 to −1.75 μm. The total dose of ~60 e^- Å^{-2} was attained by using the dose rate of ~21.97 e^- pixel^{-1} s^{-1} across 40 frames during the 3.4-s exposure time.

Images of frozen-hydrated particles of TRPV3 in the presence of 1 mM 2-APB were collected at the PNCC using SerialEM software on a Titan Krios TEM operating at 300 kV and a Gatan K3 DED camera. A total number of 25,638 micrographs were collected in the super-resolution mode with an image pixel size of 0.394 Å across the defocus range of −0.75 to −1.5 μm. The total dose of ~60 e^- Å^{-2} was attained by using the dose rate of ~20 e^- pixel^{-1} s^{-1} across 50 frames during the 1.877-s exposure time.

Image processing and 3D reconstruction

Data were processed in cryoSPARC v4.2.1 (*49*) and Relion v4.0 (*50*). Movie frames were aligned using MotionCor2 algorithm implemented in Relion 4.0. Motion-corrected micrographs were imported into cryoSPARC. Contrast transfer function (CTF) estimation was performed using the patch CTF estimation. Following CTF estimation, micrographs were manually inspected, and those with outliers in defocus values, ice thickness, and astigmatism as well as micrographs with lower predicted CTF-correlated resolution were excluded from further processing (individually assessed for each parameter relative to the overall distribution). Similar processing was used for all datasets. For example, for TRPV3 reconstituted into cNW30 nanodiscs in the presence of 1 mM THCV, the total number of 2,951,936 particles were picked using internally generated 2D templates and extracted with the 256-pixel box size and then binned to the 128-pixel box size. After several rounds of reference-free 2D classifications and heterogeneous refinements in cryoSPARC with one reference class and three automatically generated "garbage" classes, the best 237,574 particles were imported into Relion. These

particles were subjected to one round of 2D classification with 100 classes, the best classes were selected, and corresponding particles were re-extracted with the 256-pixel box size without binning. Extracted particles were refined together (C1) and subjected to CTF refinements to correct for the beam-tilt, higher order aberrations, anisotropic magnification, per particle defocus, and per micrograph astigmatism (*51*). CTF-refined particles were subjected to Bayesian polishing and CTF-refined again using the same procedure as described above. Polished and CTF-refined particles were 3D classified into 10 classes (C1). At this point, two well-defined classes were identified: one with a wide-open pore at the gate region (36,121 particles) and another with a closed pore (52,193 particles). Particles representing the two best classes were separately imported into cryoSPARC and subjected to nonuniform refinement with C4 rotational symmetry imposed. The final refinement jobs resulted in 3.68-Å resolution 3D reconstruction for the open state and 3.63-Å resolution 3D reconstruction for the inactivated state (fig. S3) that were used for model building. The reported resolution for the final maps was estimated in cryoSPARC using the gold standard Fourier shell correlation (FSC) using FSC = 0.143 criterion. The local resolution was calculated in cryoSPARC using the FSC = 0.5 criterion. Cryo-EM densities were visualized using UCSF ChimeraX (*52*).

Model building

The TRPV3 models were built in Coot (*53*) using the previously published cryo-EM structure of TRPV3 (Protein Data Bank ID: 6UW6) (*28*) as a guide. The models were tested for overfitting by shifting their coordinates by 0.5 Å (using Shake) in Phenix (*54*), refining each shaken model against the corresponding unfiltered half map, and generating densities from the resulting models in UCSF ChimeraX. The resulting models were real-space refined in Phenix 1.18 and visualized using UCSF ChimeraX and PyMOL (The PyMOL Molecular Graphics System, version 2.0 Schrödinger LLC). The pore radius was calculated using HOLE (*55*).

Ca^{2+} uptake measurements

Full-length wild-type or mutant human TRPV3 was expressed in HEK 293S cells as described above. Forty-eight hours after infection, cells were harvested by centrifugation at 550*g* for 5 min. The cells were resuspended in prewarmed Hepes-buffered saline [HBS; 118 mM NaCl, 4.8 mM KCl, 1 mM $MgCl_2$, 5 mM D-glucose, and 10 mM Hepes (pH 7.4)] containing Fura-2AM (5 μg/ml; Life Technologies) and incubated at 37°C for 45 min in the dark. The loaded cells were then pelleted by centrifugation for 5 min at 550*g*, resuspended again in prewarmed HBS, and incubated at 37°C for 30 min in the dark. The cells were subsequently pelleted and washed twice and then resuspended in HBS for experiments. The cells were kept on ice in the dark before fluorescence measurements, which were conducted using spectrofluorometer QuantaMaster 40 (Photon Technology International) at room temperature in a quartz cuvette under constant stirring. Intracellular Ca^{2+} was measured by taking the ratio of fluorescence measurements at two excitation wavelengths (340 and 380 nm) and one emission wavelength (510 nm). The excitation wavelength was switched at 200-ms intervals.

Supplementary Materials

This PDF file includes:

Figs. S1 to S7
Tables S1 and S2

REFERENCES AND NOTES

1. D. E. Clapham, TRP channels as cellular sensors. *Nature* **426**, 517–524 (2003).
2. Y. Zhao, B. M. McVeigh, V. Y. Moiseenkova-Bell, Structural pharmacology of TRP Channels. *J. Mol. Biol.* **433**, 166914 (2021).
3. A.-P. Koivisto, M. G. Belvisi, R. Gaudet, A. Szallasi, Advances in TRP channel drug discovery: From target validation to clinical studies. *Nat. Rev. Drug Discov.* **21**, 41–59 (2022).
4. H. Li, "TRP channel classification" in *Transient Receptor Potential Canonical Channels and Brain Diseases*, Y. Wang, Ed. (Springer, 2017), pp. 1–8.
5. A. M. Peier, A. J. Reeve, D. A. Andersson, A. Moqrich, T. J. Earley, A. C. Hergarden, G. M. Story, S. Colley, J. B. Hogenesch, P. McIntyre, S. Bevan, A. Patapoutian, A heat-sensitive TRP channel expressed in keratinocytes. *Science* **296**, 2046–2049 (2002).
6. M. J. Caterina, TRP channel cannabinoid receptors in skin sensation, homeostasis, and inflammation. *ACS Chem. Nerosci.* **5**, 1107–1116 (2014).
7. K. Imura, T. Yoshioka, I. Hikita, K. Tsukahara, T. Hirasawa, K. Higashino, Y. Gahara, A. Arimura, T. Sakata, Influence of TRPV3 mutation on hair growth cycle in mice. *Biochem. Biophys. Res. Commun.* **363**, 479–483 (2007).
8. I. Borbíró, E. Lisztes, B. I. Tóth, G. Czifra, A. Oláh, A. G. Szöllősi, N. Szentandrássy, P. P. Nánási, Z. Péter, R. Paus, L. Kovács, T. Bíró, Activation of transient receptor potential vanilloid-3 inhibits human hair growth. *J. Invest. Dermatol.* **131**, 1605–1614 (2011).
9. X. Cheng, J. Jin, L. Hu, D. Shen, X.-P. Dong, M. A. Samie, J. Knoff, B. Eisinger, M.-L. Liu, S. M. Huang, M. J. Caterina, P. Dempsey, L. E. Michael, A. A. Dlugosz, N. C. Andrews, D. E. Clapham, H. Xu, TRP channel regulates EGFR signaling in hair morphogenesis and skin barrier formation. *Cell* **141**, 331–343 (2010).
10. E. Yamamoto-Kasai, K. Imura, K. Yasui, M. Shichijou, I. Oshima, T. Hirasawa, T. Sakata, T. Yoshioka, TRPV3 as a therapeutic target for itch. *J. Invest. Dermatol.* **132**, 2109–2112 (2012).
11. C. Larkin, W. Chen, I. L. Szabó, C. Shan, Z. Dajnoki, A. Szegedi, T. Buhl, Y. Fan, S. O'Neill, D. Walls, W. Cheng, S. Xiao, J. Wang, J. Meng, Novel insights into the TRPV3-mediated itch in atopic dermatitis. *J. Allergy Clin. Immunol.* **147**, 1110–1114.e5 (2021).
12. M. Sulk, S. Seeliger, J. Aubert, V. D. Schwab, F. Cevikbas, M. Rivier, P. Nowak, J. J. Voegel, J. Buddenkotte, M. Steinhoff, Distribution and expression of non-neuronal transient receptor potential (TRPV) ion channels in rosacea. *J. Invest. Dermatol.* **132**, 1253–1262 (2012).
13. B. Nilius, T. Bíró, G. Owsianik, TRPV3: Time to decipher a poorly understood family member! *J. Physiol.* **592**, 295–304 (2014).
14. Z. Lin, Q. Chen, M. Lee, X. Cao, J. Zhang, D. Ma, L. Chen, X. Hu, H. Wang, X. Wang, P. Zhang, X. Liu, L. Guan, Y. Tang, H. Yang, P. Tu, D. Bu, X. Zhu, K. Wang, R. Li, Y. Yang, Exome sequencing reveals mutations in TRPV3 as a cause of Olmsted syndrome. *Am. J. Hum. Genet.* **90**, 558–564 (2012).
15. B. Mevorah, I. Goldberg, E. Sprecher, R. Bergman, A. Metzker, R. Luria, A. Gat, S. Brenner, Olmsted syndrome. *J. Am. Acad. Dermatol.* **53**, S266–S272 (2005).
16. M. Kashio, M. Tominaga, TRP channels in thermosensation. *Curr. Opin. Neurobiol.* **75**, 102591 (2022).
17. M. J. Caterina, T. A. Rosen, M. Tominaga, A. J. Brake, D. Julius, A capsaicin-receptor homologue with a high threshold for noxious heat. *Nature* **398**, 436–441 (1999).
18. K. Talavera, K. Yasumatsu, T. Voets, G. Droogmans, N. Shigemura, Y. Ninomiya, R. F. Margolskee, B. Nilius, Heat activation of TRPM5 underlies thermal sensitivity of sweet taste. *Nature* **438**, 1022–1025 (2005).
19. H. Xu, I. S. Ramsey, S. A. Kotecha, M. M. Moran, J. A. Chong, D. Lawson, P. Ge, J. Lilly, I. Silos-Santiago, Y. Xie, P. S. DiStefano, R. Curtis, D. E. Clapham, TRPV3 is a calcium-permeable temperature-sensitive cation channel. *Nature* **418**, 181–186 (2002).
20. M.-K. Chung, H. Lee, A. Mizuno, M. Suzuki, M. J. Caterina, 2-Aminoethoxydiphenyl borate activates and sensitizes the heat-gated ion channel TRPV3. *J. Neurosci.* **24**, 5177–5182 (2004).
21. H.-Z. Hu, R. Xiao, C. Wang, N. Gao, C. K. Colton, J. D. Wood, M. X. Zhu, Potentiation of TRPV3 channel function by unsaturated fatty acids. *J. Cell. Physiol.* **208**, 201–212 (2006).
22. A. S. Klein, A. Tannert, M. Schaefer, Cholesterol sensitises the transient receptor potential channel TRPV3 to lower temperatures and activator concentrations. *Cell Calcium* **55**, 59–68 (2014).
23. J. F. Doerner, H. Hatt, I. S. Ramsey, Voltage- and temperature-dependent activation of TRPV3 channels is potentiated by receptor-mediated PI(4,5)P2 hydrolysis. *J. Gen. Physiol.* **137**, 271–288 (2011).
24. M. V. Yelshanskaya, A. I. Sobolevsky, Ligand-binding sites in vanilloid-subtype TRP channels. *Front. Pharmacol.* **13**, 900623 (2022).
25. A. K. Singh, L. L. McGoldrick, A. I. Sobolevsky, Structure and gating mechanism of the transient receptor potential channel TRPV3. *Nat. Struct. Mol. Biol.* **25**, 805–813 (2018).
26. A. K. Singh, L. L. McGoldrick, L. Demirkhanyan, M. Leslie, E. Zakharian, A. I. Sobolevsky, Structural basis of temperature sensation by the TRP channel TRPV3. *Nat. Struct. Mol. Biol.* **26**, 994–998 (2019).

27. L. Zubcevic, M. A. Herzik, M. Wu, W. F. Borschel, M. Hirschi, A. S. Song, G. C. Lander, S.-Y. Lee, Conformational ensemble of the human TRPV3 ion channel. *Nat. Commun.* **9**, 4773 (2018).
28. Z. Deng, G. Maksaev, M. Rau, Z. Xie, H. Hu, J. A. J. Fitzpatrick, P. Yuan, Gating of human TRPV3 in a lipid bilayer. *Nat. Struct. Mol. Biol.* **27**, 635–644 (2020).
29. K. D. Nadezhdin, A. Neuberger, Y. A. Trofimov, N. A. Krylov, V. Sinica, N. Kupko, V. Vlachova, E. Zakharian, R. G. Efremov, A. I. Sobolevsky, Structural mechanism of heat-induced opening of a temperature-sensitive TRP channel. *Nat. Struct. Mol. Biol.* **28**, 564–572 (2021).
30. H. Shimada, T. Kusakizako, T. H. Dung Nguyen, T. Nishizawa, T. Hino, M. Tominaga, O. Nureki, The structure of lipid nanodisc-reconstituted TRPV3 reveals the gating mechanism. *Nat. Struct. Mol. Biol.* **27**, 645–652 (2020).
31. L. Zubcevic, W. F. Borschel, A. L. Hsu, M. J. Borgnia, S.-Y. Lee, Regulatory switch at the cytoplasmic interface controls TRPV channel gating. *eLife* **8**, e47746 (2019).
32. L. De Petrocellis, P. Orlando, A. S. Moriello, G. Aviello, C. Stott, A. A. Izzo, V. Di Marzo, Cannabinoid actions at TRPV channels: Effects on TRPV3 and TRPV4 and their potential relevance to gastrointestinal inflammation. *Acta Physiol.* **204**, 255–266 (2012).
33. H. Hu, J. Grandl, M. Bandell, M. Petrus, A. Patapoutian, Two amino acid residues determine 2-APB sensitivity of the ion channels TRPV3 and TRPV4. *Proc. Natl. Acad. Sci. U.S.A.* **106**, 1626–1631 (2009).
34. R. A. Pumroy, A. D. Protopopova, T. C. Fricke, I. U. Lange, F. M. Haug, P. T. Nguyen, P. N. Gallo, B. B. Sousa, G. J. L. Bernardes, V. Yarov-Yarovoy, A. Leffler, V. Y. Moiseenkova-Bell, Structural insights into TRPV2 activation by small molecules. *Nat. Commun.* **13**, 2334 (2022).
35. E. Cao, M. Liao, Y. Cheng, D. Julius, TRPV1 structures in distinct conformations reveal activation mechanisms. *Nature* **504**, 113–118 (2013).
36. Y. Gao, E. Cao, D. Julius, Y. Cheng, TRPV1 structures in nanodiscs reveal mechanisms of ligand and lipid action. *Nature* **534**, 347–351 (2016).
37. F. Zhang, K. J. Swartz, A. Jara-Oseguera, Conserved allosteric pathways for activation of TRPV3 revealed through engineering vanilloid-sensitivity. *eLife* **8**, e42756 (2019).
38. A. Neuberger, K. D. Nadezhdin, E. Zakharian, A. I. Sobolevsky, Structural mechanism of TRPV3 channel inhibition by the plant-derived coumarin osthole. *EMBO Rep.* **22**, e53233 (2021).
39. T. H. D. Nguyen, S. G. Itoh, H. Okumura, M. Tominaga, Structural basis for promiscuous action of monoterpenes on TRP channels. *Commun. Biol.* **4**, 293 (2021).
40. D. H. Kwon, F. Zhang, J. G. Fedor, Y. Suo, S.-Y. Lee, Vanilloid-dependent TRPV1 opening trajectory from cryoEM ensemble analysis. *Nat. Commun.* **13**, 2874 (2022).
41. D. H. Kwon, F. Zhang, Y. Suo, J. Bouvette, M. J. Borgnia, S.-Y. Lee, Heat-dependent opening of TRPV1 in the presence of capsaicin. *Nat. Struct. Mol. Biol.* **28**, 554–563 (2021).
42. K. D. Nadezhdin, A. Neuberger, Y. A. Nikolaev, L. A. Murphy, E. O. Gracheva, S. N. Bagriantsev, A. I. Sobolevsky, Extracellular cap domain is an essential component of the TRPV1 gating mechanism. *Nat. Commun.* **12**, 2154 (2021).
43. A. Neuberger, M. Oda, Y. A. Nikolaev, K. D. Nadezhdin, E. O. Gracheva, S. N. Bagriantsev, A. I. Sobolevsky, Human TRPV1 structure and inhibition by the analgesic SB-366791. *Nat. Commun.* **14**, 2451 (2023).
44. K. Zhang, D. Julius, Y. Cheng, Structural snapshots of TRPV1 reveal mechanism of polymodal functionality. *Cell* **184**, 5138–5150.e12 (2021).
45. A. Neuberger, K. D. Nadezhdin, A. I. Sobolevsky, Structural mechanism of TRPV3 channel inhibition by the anesthetic dyclonine. *Nat. Commun.* **13**, 2795 (2022).
46. A. Goehring, C.-H. Lee, K. H. Wang, J. C. Michel, D. P. Claxton, I. Baconguis, T. Althoff, S. Fischer, K. C. Garcia, E. Gouaux, Screening and large-scale expression of membrane proteins in mammalian cells for structural studies. *Nat. Protoc.* **9**, 2574–2585 (2014).
47. A. Neuberger, K. D. Nadezhdin, A. I. Sobolevsky, "TRPV3 expression and purification for structure determination by Cryo-EM" in *Methods in Enzymology*, vol. 652, D. L. Minor, H. M. Colecraft, Eds. (Academic Press, 2021), chap. 2, pp. 31–48.
48. A. K. Singh, L. L. McGoldrick, A. I. Sobolevsky, "Expression, purification, and crystallization of the transient receptor potential channel TRPV6" in *TRP Channels: Methods and Protocols*, A. Ferrer-Montiel, T. Hucho, Eds. (Springer, 2019), pp. 23–37.
49. A. Punjani, J. L. Rubinstein, D. J. Fleet, M. A. Brubaker, cryoSPARC: Algorithms for rapid unsupervised cryo-EM structure determination. *Nat. Methods* **14**, 290–296 (2017).
50. S. H. W. Scheres, RELION: Implementation of a Bayesian approach to cryo-EM structure determination. *J. Struct. Biol.* **180**, 519–530 (2012).
51. J. Zivanov, T. Nakane, S. H. W. Scheres, Estimation of high-order aberrations and anisotropic magnification from cryo-EM data sets in RELION-3.1. *IUCrJ* **7**, 253–267 (2020).
52. E. F. Pettersen, T. D. Goddard, C. C. Huang, E. C. Meng, G. S. Couch, T. I. Croll, J. H. Morris, T. E. Ferrin, UCSF ChimeraX: Structure visualization for researchers, educators, and developers. *Protein Sci.* **30**, 70–82 (2021).
53. P. Emsley, B. Lohkamp, W. G. Scott, K. Cowtan, Features and development of Coot. *Acta Crystallogr. D Biol. Crystallogr.* **66**, 486–501 (2010).
54. P. V. Afonine, R. W. Grosse-Kunstleve, N. Echols, J. J. Headd, N. W. Moriarty, M. Mustyakimov, T. C. Terwilliger, A. Urzhumtsev, P. H. Zwart, P. D. Adams, Towards automated crystallographic structure refinement with phenix.refine. *Acta Crystallogr. D Biol. Crystallogr.* **68**, 352–367 (2012).
55. O. S. Smart, J. G. Neduvelil, X. Wang, B. A. Wallace, M. S. Sansom, HOLE: A program for the analysis of the pore dimensions of ion channel structural models. *J. Mol. Graph.* **14**, 354–360 (1996).

Acknowledgments: We thank R. Grassucci and Z. Zhang from the Columbia University Cryo-Electron Microscopy Center for help with screening the cryo-EM grids, V. Rayaprolu and O. Davulcu from the Pacific Northwest Center for Cryo-EM (PNCC), and A. Wier from National Cryo-EM Facility at the Frederick National Laboratory for Cancer Research for help with microscope operation and data collection. **Funding:** Some of this work was performed at the Columbia University Cryo-Electron Microscopy. This research was, in part, supported by the National Cancer Institute's National Cryo-EM Facility at the Frederick National Laboratory for Cancer Research under contract 75N91019D00024. A portion of this research was supported by NIH grant U24GM129547 and performed at the PNCC at OHSU and accessed through EMSL (grid.436923.9), a DOE Office of Science User Facility sponsored by the Office of Biological and Environmental Research. A.N. is a Walter Benjamin Fellow funded by the Deutsche Forschungsgemeinschaft (DFG; German Research Foundation, 464295817). A.I.S. is supported by the NIH (R01 AR078814, R01 CA206573, R01 NS083660, and R01 NS107253). **Author contributions:** Conceptualization: K.D.N., A.N., and A.I.S. Methodology: K.D.N. and A.I.S. Investigation: K.D.N., A.N., L.S.K., I.A.T., J.K., and M.V.Y. Visualization: K.D.N. and A.I.S. Supervision: A.I.S. Writing—original draft: K.D.N. and A.I.S. Writing—review and editing: K.D.N., A.N., L.S.K., I.A.T., J.K., M.V.Y., and A.I.S. **Competing interests:** The authors declare that they have no competing interests. **Data and materials availability:** All data needed to evaluate the conclusions in the paper are present in the paper and/or the Supplementary Materials. The cryo-EM maps for have been deposited in the Electron Microscopy Data Bank with the following codes: EMD-42994 (APO), EMD-42995 ($OPEN_{THCV}$), EMD-42996 ($INACT_{THCV}$), EMD-42997 ($OPEN_{2APB}$), and EMD-42998 ($INACT_{2APB}$). The coordinates for the atomic models have been deposited in the Protein Data Bank under accession codes 8V6K (APO), 8V6L ($OPEN_{THCV}$), 8V6M ($INACT_{THCV}$), 8V6N ($OPEN_{2APB}$), and 8V6O ($INACT_{2APB}$).

Submitted 29 November 2023
Accepted 28 March 2024
Published 1 May 2024
10.1126/sciadv.adn2453